Nano Research

Open Access

Research Article

A multifunctional antibacterial nanozyme for eradicating multidrug-resistant bacteria and promoting wound repair

Jianjun Cheng[1,§], Jinghan Zhu[1,3,4,§], Jiamin Yu[2,§], Wenwen Shen[5,§], Tianfeng Wu[1], Zuozhen Yang[1], Ting Zhang[1], Junmei Zhu[1], Min Li[5], Zutao Chen[1,3,4] ✉, Xinjian Feng[1,2] ✉, and Qingzhen Han[1] ✉

[1] *Center of Clinical Laboratory and Translational Medicine, Infectious Disease Department, The Fourth Affiliated Hospital of Soochow University, Suzhou Dushu Lake Hospital, Suzhou 215000, China*
[2] *College of Chemistry, Chemical Engineering and Materials Science, Soochow University, Suzhou 215123, China*
[3] *Suzhou Key Laboratory of Pathogen Bioscience and Anti-infective Medicine, The First Affiliated Hospital of Soochow University, Suzhou 215006, China*
[4] *MOE Key Laboratory of Geriatric Diseases and Immunology, Soochow University, Suzhou 215123, China*
[5] *Institute of Biology and Medical Sciences, Soochow University, Suzhou 215123, China*
[§] *Jianjun Cheng, Jinghan Zhu, Jiamin Yu, and Wenwen Shen contributed equally to this work.*

Cite this article: *Nano Research*, **2026**, *19*, 94908625. https://doi.org/10.26599/NR.2026.94908625

ABSTRACT: The escalating global threat of multidrug-resistant (MDR) bacterial infections necessitates the development of alternative therapeutic strategies beyond traditional antibiotics. In this study, we synthesized gold-copper alloy ($AuCu_3$) nanozymes to address this challenge and investigated their catalytic efficiency, mechanisms, and interactions with the host immune system. We employed *in vitro* assays against carbapenem-resistant *Klebsiella pneumoniae* (CRKP), murine infection models, and clinical cases of otitis externa to evaluate therapeutic efficacy. Furthermore, single-cell RNA sequencing was utilized to elucidate the underlying immunomodulatory pathways. Our results demonstrate that AuCu3 nanozymes exhibit potent peroxidase-like activity, catalyzing the conversion of hydrogen peroxide (H_2O_2) into cytotoxic hydroxyl radicals. This reaction achieves broad-spectrum, irreversible bacterial elimination within three hours through synergistic membrane disruption and DNA degradation. In both animal models and clinical applications, the $AuCu_3/H_2O_2$ system effectively eradicated MDR infections and accelerated tissue repair without inducing systemic toxicity. Mechanistically, transcriptomic analysis revealed that $AuCu_3$ triggers immunometabolic reprogramming in monocytes, shifting their metabolism from glycolysis to oxidative phosphorylation. This metabolic transition enhances innate immune recruitment, while concurrent activation of copper homeostatic pathways ensures cellular equilibrium. Consequently, $AuCu_3$ represents a promising dual-action therapeutic platform that combines direct antimicrobial activity with host-directed immune modulation to combat intractable infections and promote wound healing.

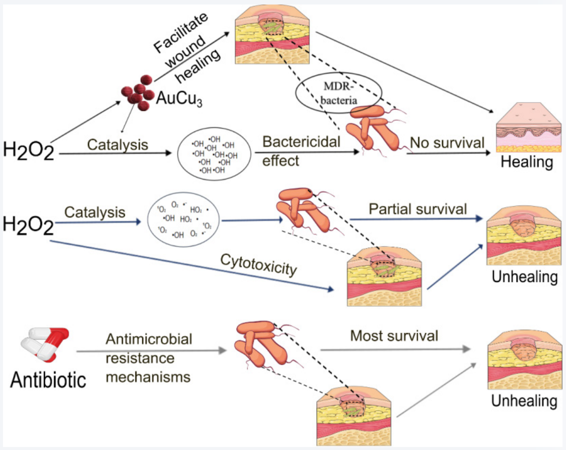

KEYWORDS: $AuCu_3$ nanoparticles, antimicrobial nanozyme, multidrug-resistant (MDR) bacteria, wound healing, monocyte

1 Introduction

The rapid global increase in antimicrobial-resistant infections has evolved into a severe public health crisis, posing a significant threat to modern healthcare system [1–3]. The overuse of antibiotics has accelerated the development of bacterial resistance, while the pace of novel antibacterial drug development lags far behind the spread of resistant strains. The World Health Organization (WHO) has classified *Carbapenem-Resistant Klebsiella pneumoniae* (CRKP) as a critical-priority "superbug", known for its multi-drug resistance, high pathogenicity, and association with significant mortality rate [4, 5]. CRKP frequently causes severe infections such as hospital-acquired pneumonia, bloodstream infections, and complicated

Received: December 24, 2025; **Revised:** March 8, 2026
Accepted: March 9, 2026

✉Address correspondence to Qingzhen Han, gyhqz2021@163.com; Xinjian Feng, xjfeng@suda.edu.cn; Zutao Chen, chenzt@suda.edu.cn

urinary tract infections. With extremely limited therapeutic options available, these infections often lead to worsened patient outcomes and impose a substantial burden on healthcare system. Therefore, the development of novel non-antibiotic strategies capable of overcoming existing resistance mechanisms while combining rapid bactericidal effects and biofilm eradication represents one of the most urgent clinical needs in the field of infectious diseases today.

Nanozymes-engineered nanomaterials with enzyme-like catalytic activity show considerable promise as therapeutic agents [6]. However, the clinical translation of many candidates is constrained by potential cytotoxicity [7, 8]. To address this challenge, we identified and synthesized gold-copper alloy nanoparticles ($AuCu_3$) through systematic preliminary screening. The obtained $AuCu_3$ nanoparticles possess a unique electronic structure, atomic-level ordering, and high stability, which collectively enable tunable catalytic properties. Furthermore, their low cytotoxicity and strong peroxidase-like (POD-like) activity make them highly advantageous for antimicrobial applications [9, 10]. This study aimed to go beyond the early and often limited conclusions of earlier studies. These studies had problems like: (1) relying on model strains (like *E. coli* ATCC25922 and *S. aureus* ATCC25923) tested in non-clinical buffers that do not reflect real-life conditions; (2) not testing for efficacy against high-priority resistant pathogens (like CRKP and methicillin-resistant *Staphylococcus aureus* (MRSA)), which raised concerns about refractory clinical infections; (3) not examining whether the effects were bactericidal or bacteriostatic; (4) not looking into reusability; and (5) lacking *in vivo* data on antibacterial efficacy, other possible effects, and host toxicity.

This study systematically evaluates the bactericidal potency, speed, spectrum, mechanisms, and recyclability of $AuCu_3$ against clinically isolated resistant strains. We conducted a comprehensive assessment encompassing *in vitro* cultures under nutrient-rich conditions, animal models of skin wound infection, and a human clinical case of otitis externa. Our findings demonstrate that the nanozyme exhibits excellent biocompatibility with no detectable toxicity, thereby establishing a solid foundation for its development as a novel therapeutic agent.

2 Experimental

2.1 Synthesis and structural analysis of $AuCu_3$

$AuCu_3$ was synthesized according to the method described in Refs. [10, 11]. 1.51 g of copper acetate ($Cu(COO)_2{\cdot}H_2O$) and 1 g of chloroauric acid tetrahydrate ($HAuCl_4{\cdot}3H_2O$) were dissolved in 25 mL of deionized water under an Ar atmosphere with stirring for 20 min. 10 mL of 0.05 M sodium borohydride ($NaBH_4$) aqueous solution was then added. After continuous stirring under Ar for 2 h, the mixture was washed with acetone by centrifugation several times and dried overnight at 50 °C under vacuum. The dried powder was calcined at 300 °C for 2 h under a nitrogen atmosphere at a heating rate of 5 °C/min to obtain $AuCu_3$ nanocrystals. The particle size was observed using a scanning electron microscope (SEM) (SU8010, Hitachi, Japan), and selected area electron diffraction and elemental distribution were detected using a transmission electron microscope (TEM) (Talos F200X G2, Thermo Fisher Scientific).

2.2 Assessment of peroxidase-like activity of $AuCu_3$

The catalytic generation of hydroxyl radicals (·OH) from H_2O_2 was used to confirm the peroxidase-like activity of the synthesized $AuCu_3$. During the antibacterial process, the synthesized $AuCu_3$ also exhibits peroxidase-like activity, which is confirmed by detecting hydroxyl radicals in the system. Groups were set up with H_2O_2 alone (5, 10, 50, 100 mM), $H_2O_2/AuCu_3$ (5, 10, 50, 100 mM/50 μg/mL), and polymyxin-resistant, carbapenem-resistant *Klebsiella pneumoniae* (PR-CRKP) + $H_2O_2/AuCu_3$ (5, 10, 50, 100 mM/50 μg/mL). After adding the reagents, the mixtures were reacted for 20 min, followed by the addition of 8 mM 5,5-dimethyl-1-pyrroline *N*-oxide (DMPO) to trap hydroxyl radicals. The samples were then analyzed using an electron spin resonance (ESR) spectrometer (JES-X320, JEOL, Japan) to detect the hydroxyl radical signal peaks.

2.3 Cytotoxicity evaluation of $AuCu_3$

AML12 cells were seeded into 96-well plates at a density of 5×10^3 per well, with five replicates per group. After overnight incubation to allow cell adherence, the culture medium was replaced with a series of H_2O_2 concentrations, 50 μg/mL $AuCu_3$, and mixtures thereof. At 0, 24, and 48 h after addition, the Cell Counting Kit-8 (CCK-8) assay was performed: The culture medium was replaced with 100 μL of fresh medium containing 10 μL of CCK-8 reagent. The plates were incubated at 37 °C for 1 h, and the absorbance at 450 nm was measured.

2.4 Long-term bactericidal test of $AuCu_3$ against PR-CRKP

Clinical isolates of PR-CRKP (strain Kpn-2024-0875) were cultured on blood agar plates at 35 °C with 5% CO_2 for 24 h. The bacterial colonies were scraped and suspended in physiological saline to achieve a turbidity of 3 McFarland units. 3 mL of Luria-Bertani (LB) broth were inoculated with 7.6×10^6 CFU/mL of bacteria. Groups were set up as follows: growth control, H_2O_2 alone (1000, 5000, 10,000, 50,000 μM), $AuCu_3/H_2O_2$ (various concentrations/10 μg/mL), and $AuCu_3/H_2O_2$ (various concentrations/50 μg/mL). The tubes were incubated in a shaking incubator at 35 °C and 200 rpm for 24 and 48 h. The results were observed and photographed, with the experiment repeated three times.

2.5 Rapid bactericidal test of $AuCu_3$ against multiple clinical bacteria

Clinical isolates of various pathogens were cultured on blood agar plates at 35 °C with 5% CO_2 for 24 h. The bacterial colonies were scraped and suspended in physiological saline to achieve a turbidity of 0.5 McFarland units. The suspensions were inoculated into 3 mL of liquid culture medium at a concentration of 5×10^5 CFU/mL. The treatment conditions included untreated control, H_2O_2 alone, $AuCu_3$ alone, and $AuCu_3/H_2O_2$ combinations. The cultures were incubated in a shaking incubator at 35 °C and 200 rpm for 3 h. A 20-μL aliquot was diluted 50 times, and 20 μL of the diluted sample was spread onto nutrient agar plates using a spreader. The plates were incubated at 35 °C for 24 h, and colony counts were performed. The effective concentration was determined based on the statistical differences in colony counts compared to the control. Each strain was tested in triplicate, with the experiment repeated three times. The clinical pathogens used included *Escherichia coli* (ATCC25922 and Eco-2025-0012), *Klebsiella pneumoniae* (Kpn-2024-0875 and Kpn-2025-0118), *Staphylococcus aureus* (ATCC25923 and Sau-2025-0193), *Acinetobacter baumannii* (Aba-

2024-0527 and Aba-2024-0878), *Pseudomonas aeruginosa* (ATCC27853 and Pae-2025-0092), and two strains of *Burkholderia cepacia* (Bce-2025-0001 and Bce-2025-0002), covering both sensitive and drug-resistant strains.

2.6 Reusability test of $AuCu_3$

A 3-mL volume of LB broth was treated with 10 mM H_2O_2 and 50 μg/mL $AuCu_3$ for 24 h. The mixture was then centrifuged at 3000 rpm for 10 min to remove the culture medium, and the precipitate was washed three times with fresh LB broth and transferred to a new culture tube. The tube with 3 mL fresh broth was inoculated with a 0.5 McFarland unit suspension of PR-CRKP prepared in advance, and the cultures were performed as described above. The treatment groups included blank controls without bacterial inoculation, untreated controls, 500 μM fresh H_2O_2, 500 μM fresh H_2O_2 + 50 μg/mL fresh $AuCu_3$, 500 μM fresh H_2O_2 + 50 μg/mL recovered $AuCu_3$, and recovered $AuCu_3$ alone. After 3 h of culture, the samples were transferred to agar plates for solid culture for 24 h, and the live bacterial counts were observed. The recycled $AuCu_3$ nanozymes were analyzed and characterized by aberration-corrected electron microscopy and high-resolution TEM.

2.7 Mechanism of bactericidal action of nanozyme

Clinical isolates of Kpn-2024-0875, Sau-2025-0193, and ATCC25923 were cultured on blood agar plates at 35 °C with 5% CO_2 for 24 h. The bacterial colonies were scraped and suspended in physiological saline to achieve a turbidity of 10 McFarland units. The suspensions were cultured in LB broth for 3 h as described above, with the following treatment groups: control, H_2O_2 alone (5000 μM), and H_2O_2 (5000 μM)/$AuCu_3$ (50 μg/mL).

2.7.1 SEM observation of bacterial morphology

The bacterial suspensions were centrifuged at 10,000 rpm to collect the precipitates. The precipitates were fixed in 2.5% glutaraldehyde in PBS overnight at 4 °C. The next day, the fixed samples were washed three times with phosphate buffered saline (PBS), followed by gradient dehydration with 50%, 70%, 80% ethanol, 2:1 ethanol and acetone, 1:1 ethanol and acetone, and pure acetone for approximately 30 min each. The samples were then dropped onto titanium stubs for SEM, freeze-dried for 2 h, and sputter-coated with gold to enhance conductivity. The samples were observed and photographed using an SEM (SU8010, Hitachi, Japan).

2.7.2 DNA damage analysis

The bacterial suspensions were centrifuged at 10,000 rpm to collect the precipitates. Genomic DNA was extracted from the bacterial samples using an Ezup Column Bacteria Genomic DNA Purification Kit (Sangon Biotech, CAS: B528131, China) according to the manufacturer's instructions. The genomic DNA was then analyzed by agarose gel electrophoresis to observe the DNA band patterns.

2.8 *In vivo* wound healing and anti-infection assessment

A murine model was established to evaluate the therapeutic efficacy of the treatments. Twenty C57BL/6 mice were randomly allocated into four experimental groups (n = 5 per group): (a) uninfected control, (b) PR-CRKP-infected and untreated, (c) the nanozyme group ($AuCu_3$), (d) the H_2O_2 group, and (e) the combination group ($AuCu_3$+H_2O_2). Following anesthesia with tribromoethanol, full-thickness skin wounds were created on the dorsum of each mouse. The wounds were subsequently infected with approximately 1×10^8 CFU of PR-CRKP bacterial strains. Treatments were administered topically once daily for seven consecutive days. Specifically, Group (c) received 10 μL of $AuCu_3$ nanozyme (10 ng/μL), Group (d) received 500 mM H_2O_2, and Group (e) received a combination of both agents at the same concentrations; all treatments were applied to the infected wound sites. The control group received no therapeutic intervention after infection. Wound closure and morphological changes were monitored and documented daily throughout the treatment period. On day 8 post-treatment, all mice were euthanized. Skin wound tissues and liver samples were harvested for histological analysis via hematoxylin and eosin (H&E) staining. All animal experiments were approved by the Institutional Animal Care and Use Committee of the Fourth Affiliated Hospital of Soochow University (251224), and were conducted in accordance with the relevant guidelines and regulations.

2.9 Clinical case report and treatment regimen

A single clinical case of bilateral bacterial otitis externa was documented. The condition initially presented in the right ear on July 22, 2025, with symptoms of pain and swelling, which partially alleviated following povidone-iodine disinfection. Subsequently, the left ear became affected on July 28, 2025, with symptoms progressing in severity. By July 30, a clear clinical disparity was evident: the right ear exhibited mild symptoms (a minor furuncle with mild tenderness), while the left ear presented with severe manifestations, including two distinct masses and one ulcer, accompanied by significant pain. A differential topical treatment regimen was initiated on July 31. The severely affected left ear was treated topically three times daily with 50 μg/mL $AuCu_3$ plus 500 μM H_2O_2, while the milder right ear received 500 μM H_2O_2 alone on the same schedule. Clinical outcomes, including symptom resolution, tissue swelling, and canal patency, were assessed daily. Microbiological culture swabs were obtained from both ears at the conclusion of the three-day treatment period to evaluate the bacterial load and flora composition. Ethical note: The subject involved in this clinical case was one of the co-authors of this study, who voluntarily consented to participate. The entire investigative process was carried out under the supervision and with the assistance of the other authors.

2.10 Single-cell sequencing

This research consists of five core steps. First, single-cell suspensions were adjusted to a concentration of 1000–2000 cells/μL, and single-cell RNA libraries were constructed using the DNBelab C Series High-Throughput Single-Cell RNA Library Preparation Kit V3.0, with 25,000–30,000 cells loaded per sample, in accordance with MGI's standard protocols. Second, libraries were sequenced as 150-bp paired-end reads on the DNBSEQ-T7 platform; the resulting FASTQ data were aligned to the human hg38 genome via the STAR algorithm, processed using Cell Ranger to generate gene-barcode matrices with unique molecular identifiers (UMIs), and subjected to quality control in Seurat. Quality control filters excluded cells with fewer than 200 detected genes, genes expressed in fewer than 3 cells, or cells with more than 10% mitochondrial gene content. Third, unsupervised cell clustering was performed using the 2000 most differentially expressed genes—excluding cell cycle-, mitochondrial-, and ribosomal-related genes—via principal component analysis (PCA) (top 50 components), followed by Seurat's FindNeighbors and FindClusters functions. Cell types were annotated using canonical marker genes and Seurat's FindAllMarkers function. Fourth, subcluster analysis of major cell populations entailed PCA on the top differentially expressed genes, unsupervised clustering via *k*-means, and marker gene identification using Seurat's FindMarkers function. Unsupervised clustering at a resolution of 1 identified 32 distinct cell clusters. These clusters were annotated into ten major cell types (e.g., B cells, $CD4^+$ T cells, $CD8^+$ T cells, NK cells, monocytes) based on the expression of canonical marker genes [12, 13]. Finally, pathway enrichment analysis was conducted by first utilizing FindMarkers to identify differentially expressed mRNAs between comparison groups, followed by clusterProfiler to detect enriched Kyoto Encyclopedia of Genes and Genomes (KEGG) pathways and Gene Ontology (GO) biological processes (Q-value < 0.05).

2.11 Statistical and analytical methods

GraphPad Prism 8.0 was applied for statistical analysis. The bacterial CFU/mL in each group were presented as mean ± standard deviation (SD). Statistical analysis between comparable groups was performed using *t*-test, with $P < 0.05$ indicating significant difference.

3 Results and discussion

3.1 $AuCu_3$ nanoparticles with potent peroxidase-like activity and excellent biocompatibility

$AuCu_3$ nanoparticles were synthesized using a one-step co-reduction method (Fig. 1(a)). High-resolution transmission electron microscopy (HRTEM) revealed uniform spherical particles with a size of approximately 200 nm (Fig. 1(b)). The morphology and lattice fringes of the $AuCu_3$ were observed by TEM (Figs. 1(c) and 1(d)). Selected area electron diffraction (SAED) and energy-dispersive X-ray spectroscopy (EDS) mapping verified the composition of the atomically ordered $AuCu_3$ alloy (Figs. 1(e)–1(i)). As shown in Fig. 1(j), all of the diffraction peaks of the sample are consistent with the $AuCu_3$ intermetallic phase [11]. The POD-like activity of $AuCu_3$ was proven by ESR spectroscopy using DMPO as a spin trap, which detected ·OH generated from H_2O_2 decomposition. The intensity of the ·OH signal correlated with the substrate concentration (Fig. 1(k)), and the catalytic kinetics were consistent with an enzyme-like mechanism [14]. As shown in Fig. 1(l), more than 500 μM H_2O_2 exhibited pronounced cytotoxicity of mouse normal liver cells (AML12) ($P < 0.01$). In contrast, $AuCu_3$ at the highest concentration tested (50 μg/mL) exhibited no significant cytotoxicity (Fig. 1(m)). In addition, the release kinetics of copper and gold ions were monitored via inductively coupled plasma mass spectrometry (ICP-MS). In the antibacterial system comprising 50 μg/mL $AuCu_3$ and 5 mM H_2O_2, only trace amounts of copper and gold were released over 24 h (Table S1 in the Electronic Supplementary Material (ESM)), concentrations far below the cytotoxic thresholds reported in the literature [15].

These results suggest that $AuCu_3$ itself exhibits excellent biocompatibility, with the primary source of toxicity in the catalytic system being the substrate H_2O_2 [16, 17]. Collectively, these findings demonstrate that the synthesized $AuCu_3$ nanoparticles possess potent POD-like activity and outstanding biocompatibility, making them promising candidates for biomedical applications.

3.2 Complete killing of PR-CRKP by $AuCu_3/H_2O_2$ system in nutrient-rich conditions

To better simulate realistic infection conditions, all antibacterial assays were performed in nutrient-rich LB broth, rather than in a nutrient-poor buffer. This environment supports robust bacterial proliferation, thereby requiring that the bactericidal efficacy surpasses the innate growth rate of the bacteria [18]. The target pathogen was a clinically relevant, pan-drug resistant PR-CRKP isolate (strain Kpn-2024-0875), demonstrating resistance to both carbapenems and polymyxins (drug sensitivity results are shown in Tables S2 and S3 in the ESM). To assess the potentiating effect of $AuCu_3$, we examined the synergistic antibacterial activity between $AuCu_3$ nanoparticles and H_2O_2 in an LB broth culture medium (Fig. 2(a)). High concentrations of H_2O_2 (≥ 10 mM) could completely inhibit the growth of PR-CRKP after 24 h (clear culture medium), primarily through oxidative damage caused by the decomposition of H_2O_2. In contrast, the $AuCu_3/H_2O_2$ system (50 μg/mL $AuCu_3$ and 5 mM H_2O_2) completely eradicated PR-CRKP, demonstrating significantly enhanced antibacterial efficacy compared to H_2O_2 alone (Fig. 2(b)). The McFarland turbidity assay revealed that the clarified tube was virtually clear, showing a striking contrast to the control. In contrast, had there been any surviving bacteria due to incomplete eradication, prolonged incubation would be expected to allow their growth, thus no significant turbidity difference would be observed (Fig. 2(c)). These results confirm the catalytic enhancement effect of $AuCu_3$, which generates ·OH from H_2O_2 to kill bacteria [19], without interference from complex components in the culture medium (e.g., peptone and yeast extract).

The limited efficacy of conventional antibiotics, which achieve bactericidal rates of 90%–99.9%, reflects their non-sterilizing nature and contributes to the frequent emergence of resistance and recurrent infections [20, 21]. The $AuCu_3$-based strategy overcomes this fundamental limitation. Its key advantage lies in achieving complete bacterial eradication and maintaining a sterile environment, thereby preventing regrowth and effectively blocking the development of resistance, as well as the relapse and spread of infection. The non-toxic $AuCu_3$ enables effective sterilization at significantly lower concentrations of H_2O_2, reducing the explosion hazards and biological toxicity associated with high concentrations of H_2O_2.

3.3 Rapid bactericidal capability of $AuCu_3/H_2O_2$ against PR-CRKP and MRSA

The efficacy of conventional antibiotics is limited by their slow mechanism of action, which depends on bacterial metabolism and can require over 8 h. This delay underscores the critical need for rapidly acting antimicrobials. Addressing this, we investigated the $AuCu_3/H_2O_2$ system and identified a rapid, 3-h bactericidal effect against two representative clinical drug-resistant isolates in LB broth (Fig. 3(a)). Meanwhile, high concentrations of reactive oxygen species (ROS) were observed in the bacterial suspension (Fig. 1(k)). MRSA is another clinically prevalent, Gram-positive, drug-resistant pathogenic bacterium [5, 22]. PR-CRKP (KP-2024-0875) and MRSA (Sau-2025-0193, drug sensitivity shown in Tables S2 and S3 in the ESM) were utilized to assess the time-kill kinetics of the $AuCu_3$ nanozyme. The $AuCu_3/H_2O_2$ combination demonstrated superior antibacterial activity (Figs. 3(b)(1)–3(b)(4)), compared to the groups of H_2O_2 alone, $AuCu_3$ alone, or

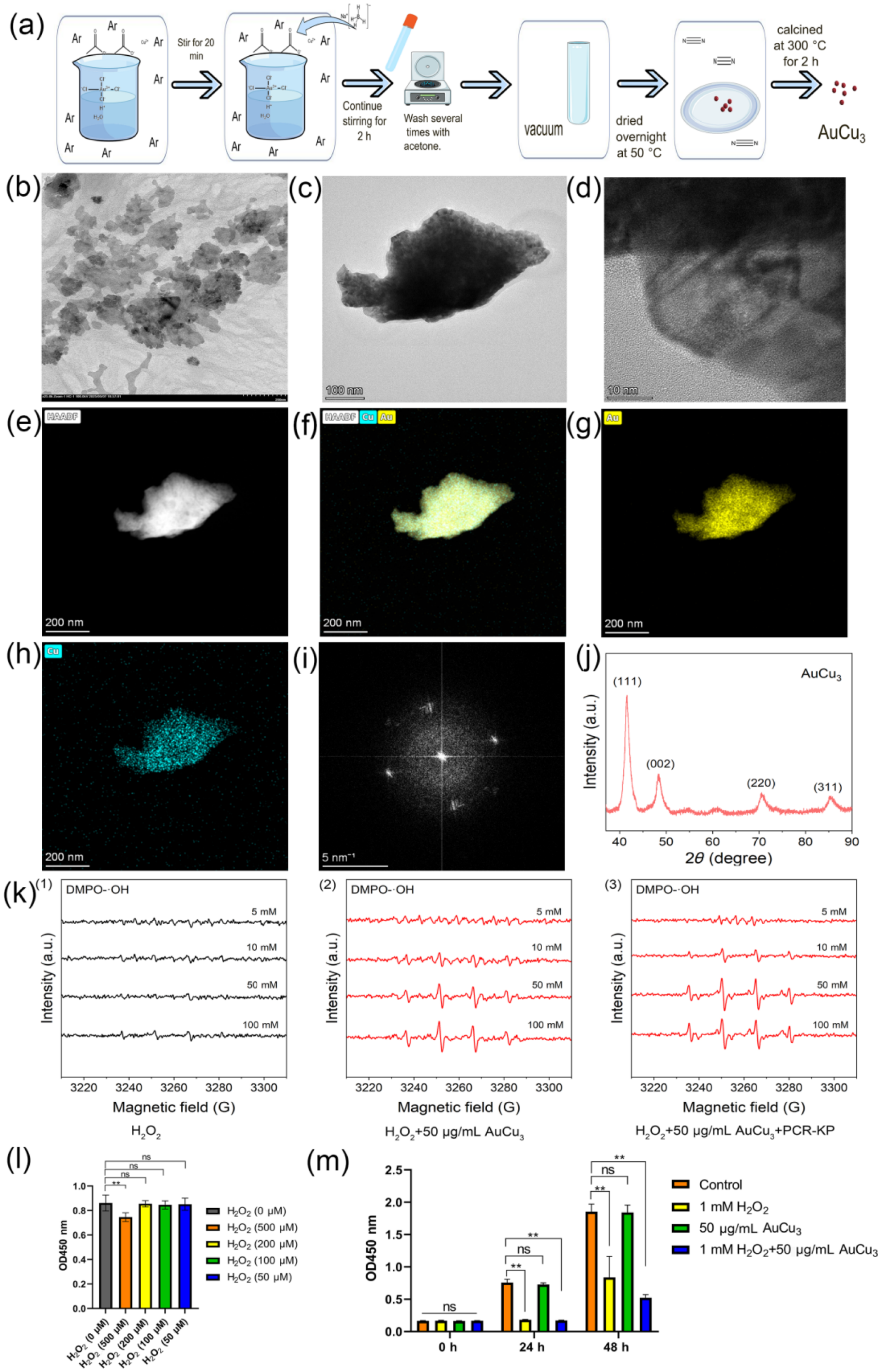

Figure 1 Synthesis and characterization of $AuCu_3$ nanoparticles. (a) Schematic illustration of the synthesis process of $AuCu_3$ nanozyme. (b) SEM image of $AuCu_3$ (non-high resolution). (c) Typical TEM image of intermetallic $AuCu_3$. (d) High-resolution TEM image of $AuCu_3$; (e) high-angle annular dark-field scanning transmission electron microscopy (HAADF-STEM) image of intermetallic $AuCu_3$; (f) energy dispersive spectroscopy (EDS) mapping of $AuCu_3$. (g) The EDS mapping of Au corresponds to the square region shown in panel (e). (h) The EDS mapping of Cu corresponds to the square region shown in panel (e). (i) Diffraction patterns of $AuCu_3$ nanoparticles. (j) X-ray diffraction pattern of $AuCu_3$ nanozyme particles. (k) ESR spectra of DMPO-trapped ·OH signals; (l) effects of different H_2O_2 concentrations on the activity of AML12 cells (OD_{450} nm absorbance); (m) CCK-8 assay results (comparison of AuCu3, H_2O_2, and $AuCu_3$+H_2O_2).

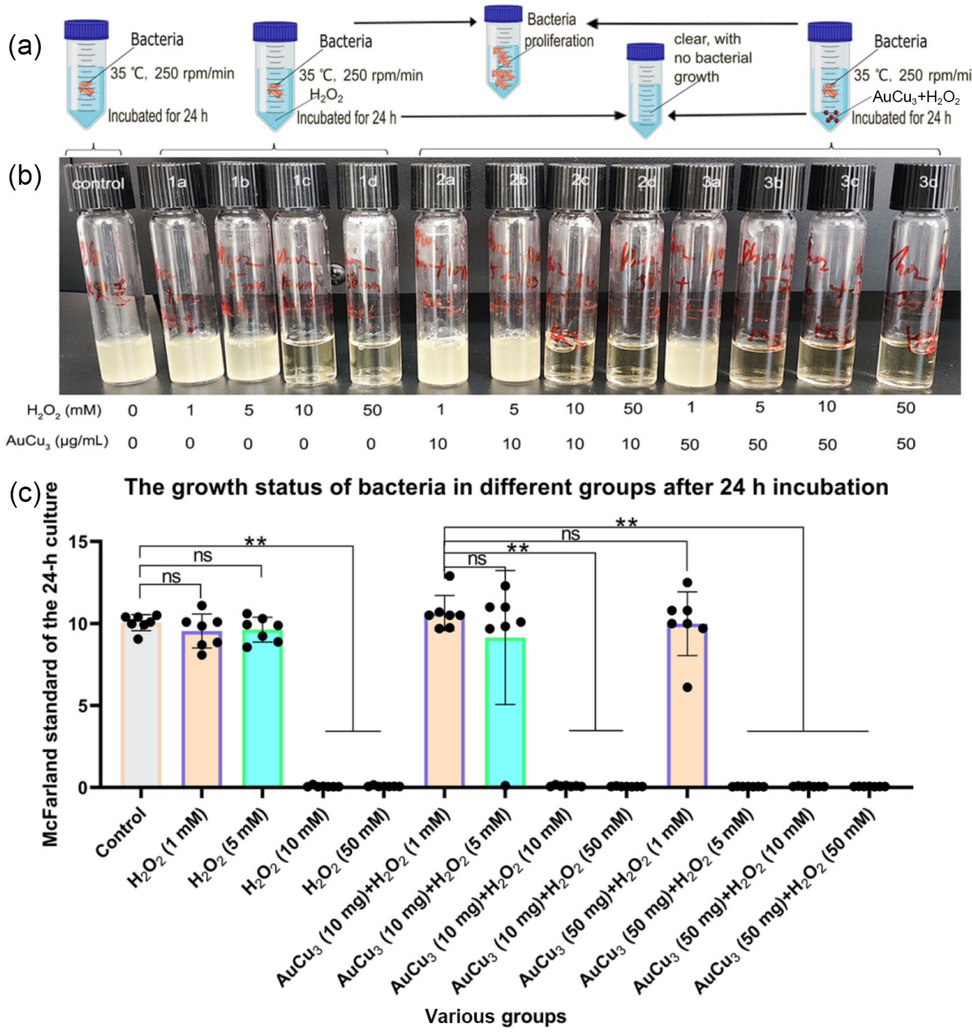

Figure 2 The complete bactericidal effect of $AuCu_3/H_2O_2$ on Kpn-2024-0875 in LB broth. (a) Schematic diagram of the bactericidal assay procedure; (b) the turbidity of the culture medium after 24 h of incubation under different conditions (as indicated in the figure), with clarity indicating no visible bacterial growth to the naked eye; (c) McFarland turbidity and statistical results of each group after 24 h incubation, ns: no significance, $P > 0.05$, $^{**}P < 0.01$.

meropenem, the untreated control (Figs. 3(b)(5)–3(b)(11)). Statistical analysis confirmed that these enhancements were significant (Fig. 3(d)). For MRSA, at 50 μg/mL $AuCu_3$ and 1000 μM H_2O_2, almost no live bacteria were detected, achieving 100% killing (Figs. 3(c) and 3(e)). These results demonstrate that $AuCu_3$ exhibits a significant antibacterial effect within 3 h, characterized by its rapid bactericidal action. Interestingly, the $AuCu_3$ nanoparticles used in the bactericidal experiments were recovered through centrifugation and washing, and upon re-adding H_2O_2, they still retained over 80% bactericidal efficiency (Fig. S1 in the ESM). Additionally, ROS generation assays and TEM characterization demonstrated that the recovered $AuCu_3$ nanozymes retained their key physicochemical properties with minimal alteration (Fig. S2 in the ESM). Compared to traditional biological enzymes, this reusable property—where the nanoparticles are not consumed during the process—could significantly reduce costs, whether applied in hospital environmental disinfection or as nano-therapeutic agents for *in vivo* antibacterial use.

The global antibiotic crisis, characterized by the relentless rise of antimicrobial resistance and the emergence of pan-drug-resistant Gram-negative pathogens such as PR-CRKP, is exacerbated by the limitations of conventional antibiotics. These antibiotics often suffer from slow action, high relapse rates, and adverse side effects, making it difficult to keep pace with the rapid evolution of bacteria, particularly in critically ill intensive care unit (ICU) patients [23]. In this context, $AuCu_3$ nanozymes, which exert rapid complete bactericidal effects through physiochemical mechanisms, represent a highly promising alternative. Their reusability further minimizes the risk of accumulation from repeated use and offers a more cost-effective solution.

3.4 Broad-spectrum bactericidal activity of $AuCu_3/H_2O_2$ with optimal concentration

Clinically, polymicrobial infections involving two or more drug-resistant species are common. The use of multiple antibiotics exacerbates side effects and healthcare costs, making broad-spectrum efficacy without specificity a critical advantage of novel nano-agents. Therefore, the antibacterial effects of the $AuCu_3/H_2O_2$ system were further tested against common Gram-positive (G^+) and Gram-negative (G^-) pathogens, including standard strains and clinical isolates with sensitive and drug-resistant phenotypes. $AuCu_3/H_2O_2$ exhibited significant antibacterial effects against all tested strains (Table 1), including *E. coli* (ATCC25922 and Eco-2025-0012), *K. pneumoniae* (Kpn-2024-0875 and Kpn-2025-0118),

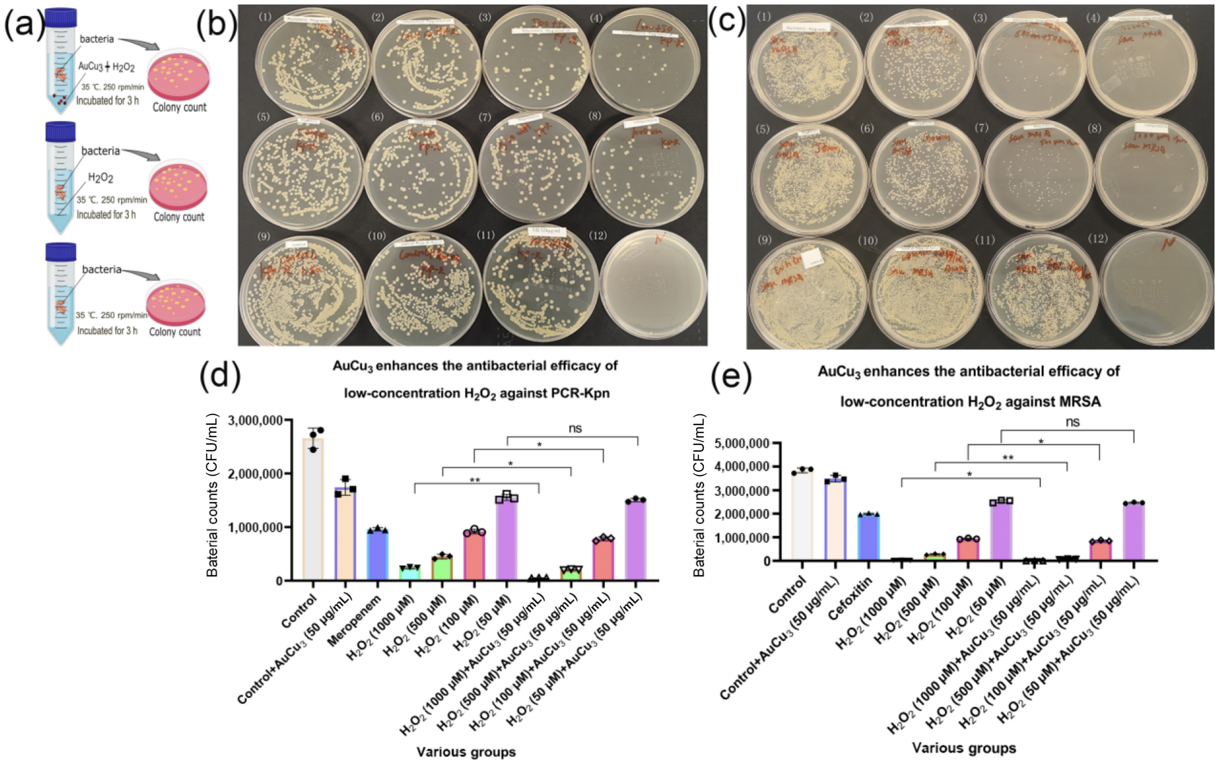

Figure 3 Rapid bactericidal capability of $AuCu_3/H_2O_2$ against PR-CRKP and MRSA. (a) Schematic diagram of the rapid bactericidal assay; (b) bactericidal effects of $AuCu_3/H_2O_2$ (3 h) versus meropenem (3 h) on Kpn-2024-0875 (viable cell counts); (c) bactericidal effects of $AuCu_3/H_2O_2$ (3 h) on Sau-2025-0193 (SA-001) (viable cell counts). Groups (1)–(4) were treated with 50 μg/mL $AuCu_3$ and H_2O_2 at concentrations of 50, 100, 500, and 1000 μM, respectively. Groups (5)–(8) were treated with H_2O_2 at concentrations of 50, 100, 500, and 1000 μM. Group (9): Growth control. Group (10): Control with 50 μg/mL $AuCu_3$ alone. Group (11): Antibiotic control (Meropenem for panel (b), Cefoxitin for panel (c)). Group (12): Blank control (culture medium only). (d) and (e) Bacterial CFU counts at 3 h post-incubation, enumerated through AI colony counter (Yida Junxi, China). When colonies were too numerous to count (TNTC), a value of 1000 colonies/plate was uniformly assigned. CFU counts are expressed as mean ± SD. ns: no significance, $P > 0.05$, $^*P < 0.05$, $^{**}P < 0.01$.

S. aureus (ATCC25923 and Sau-2025-0193), *A. baumannii* (Aba-2024-0527 and Aba-2024-0878), *P. aeruginosa* (ATCC27853 and Pae-2025-0092), and two strains of *B. cepacia* (Bce-2025-0001 and Bce-2025-0002) ($P < 0.05$). The minimum effective H_2O_2 concentration combined with 50 μg/mL $AuCu_3$ required for significant antibacterial activity varied among different bacterial species/strains. For example, 500 μM H_2O_2 was needed for *E. coli* ATCC25922, while 100 μM was sufficient for *S. aureus* and *B. cepacia*. However, overall, a combination of 50 μg/mL $AuCu_3$ and 500 μM H_2O_2 was effective against almost all tested strains. These results demonstrate that $AuCu_3/H_2O_2$ exhibits significant bactericidal effects against common clinical bacteria, surpassing limitations related to bacterial species and drug susceptibility. However, the minimum inhibitory concentration of $AuCu_3/H_2O_2$ may vary slightly depending on the bacterial strain. This difference is likely attributed to variations in bacterial cell wall composition [24, 25].

Transcending the limitations imposed by bacterial species and drug susceptibility profiles is a key advantage of the Au-Cu nanozyme-based strategy. The broad-spectrum efficacy against a diverse panel of Gram-positive and Gram-negative bacteria including ESKAPE pathogens (*Enterococcus faecium*, *Staphylococcus aureus*, *Klebsiella pneumoniae*, *Acinetobacter baumannii*, *Pseudomonas aeruginosa*, and *Enterobacter* species), a group of MDR bacteria highlighted by the WHO [5, 26], as well as notoriously resilient species like *B. cepacia* [27], underscores its potential as a universal antibacterial agent. Although the minimum effective H_2O_2 concentration varies among different strains, likely due to differences in cell wall composition [28], this does not diminish its overall effectiveness, as a universally effective concentration combination has been identified. Furthermore, the rapid bactericidal action within three hours addresses a critical clinical need for fast-acting agents, especially in sepsis and other acute infections where delays in effective therapy correlate with increased mortality [29].

3.5 Mechanism of bactericidal action of $AuCu_3/H_2O_2$ system: membrane disruption and DNA degradation

To elucidate the unique bactericidal mechanism of the $AuCu_3/H_2O_2$ system, which differs fundamentally from that of H_2O_2 alone, we performed SEM and DNA assays (Fig. 4(a)). Compared with the control (Fig. 4(b)), the morphology of PR-CRKP (KP-2024-0875) treated with H_2O_2 alone (5 mM) showed only mild damage (Fig. 4(c)). In contrast, the $AuCu_3/H_2O_2$ treatment caused severe destruction of bacterial morphology, with extensive, irreversible cell membrane rupture, pores, and leakage of cytoplasmic contents (Fig. 4(d)). Agarose gel electrophoresis (Fig. 4(e)) showed that, compared with the control, 500 μM H_2O_2 alone had a significant DNA degradation effect on the standard *S. aureus* strain (ATCC25923), but a weaker effect on the clinical drug-resistant strain MRSA. In contrast, the $AuCu_3/H_2O_2$ system (50 μg/mL/500 μM) completely degraded the genomic DNA of both PR-CRKP and MRSA after 3 h of treatment (almost no bands were visible, with only diffuse smearing).

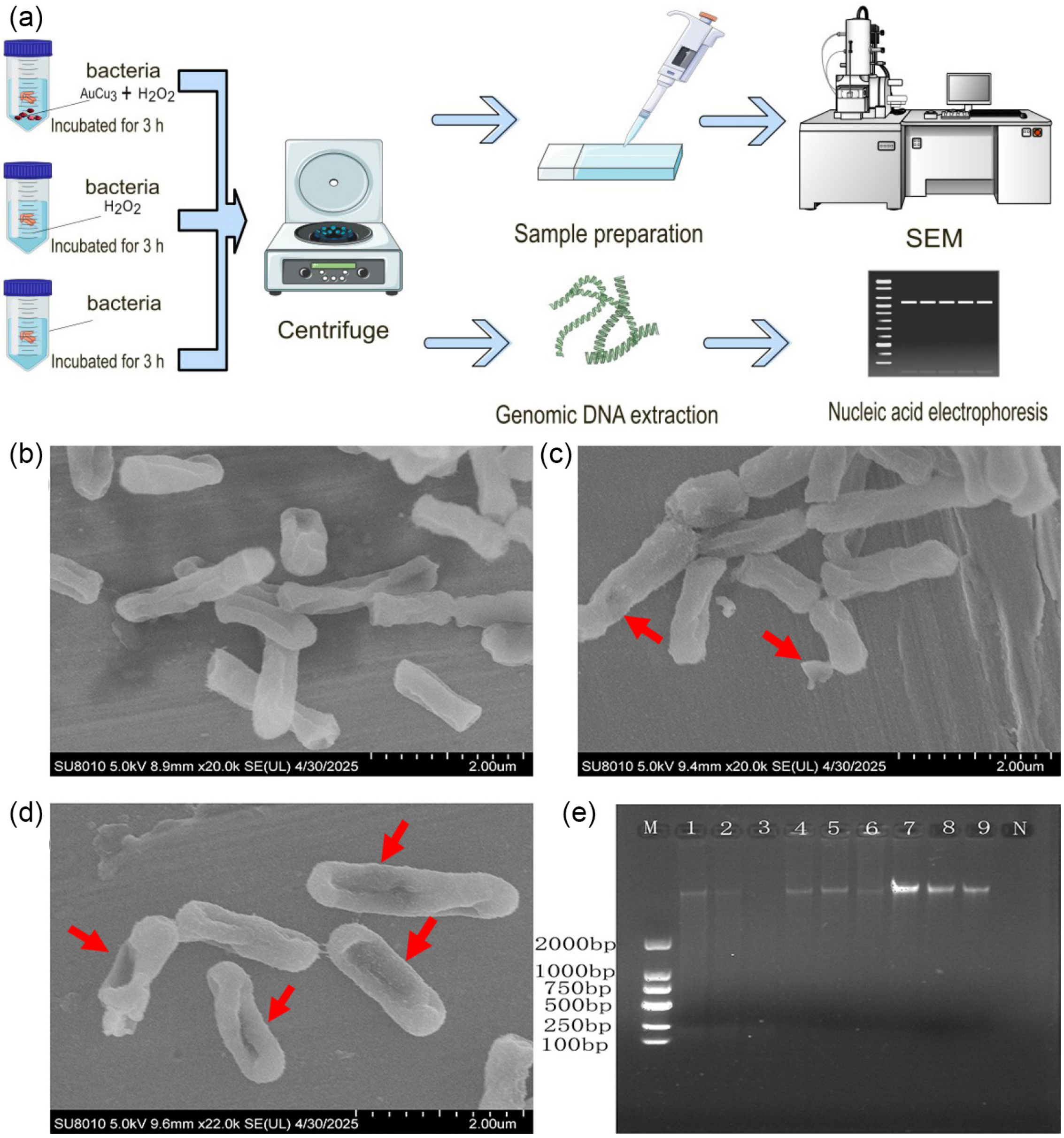

Figure 4 Membrane disruption and DNA degradation of PR-CRKP and MRSA by $AuCu_3/H_2O_2$. (a) Schematic diagram investigating the mechanism of bacterial killing. SEM images of Kpn-2024-0875: (b) untreated control, (c) treated with 15,000 μM H_2O_2, (d) treated with 50 μg/mL $AuCu_3$ + 15,000 μM H_2O_2. (e) Agarose gel electrophoresis of bacterial genomic DNA. Lanes 1–3 from MRSA (ATCC 25923), Lane 1: Control, Lane 2: 15,000 μM H_2O_2, Lane 3: 50 μg/mL $AuCu_3$ + 15,000 μM H_2O_2; Lanes 4–6 from MRSA (Sau-2025-0193), Lane 4: Control, Lane 5: 15,000 μM H_2O_2, Lane 6: 50 μg/mL $AuCu_3$ + 15,000 μM H_2O_2; Lanes 7–9 from PR-CRKP (Kpn-2024-0875), Lane 7: Control, Lane 8: 15,000 μM H_2O_2, Lane 9: 50 μg/mL $AuCu_3$ + 15,000 μM H_2O_2. M: DNA marker. N: Blank control (no nucleic acid).

Together, these data reveal that the $AuCu_3/H_2O_2$ synergy operates through a catalytic burst mechanism. Upon contact, $AuCu_3$ rapidly decomposes H_2O_2, generating a massive local ROS flux that overwhelms the bacterial antioxidant buffering capacity. This ROS surge induces extensive cell wall rupture and irreversible lysis, preventing any metabolic recovery. This catalytic mode may be generalizable to nanozymes; however, catalytic efficiency emerges as the critical differentiator. $AuCu_3$ maintains robust bactericidal efficacy in complex, nutrient-rich bacterial growth media, where ROS typically undergo rapid scavenging—unlike the rapid quenching observed in simple physiological saline. This environmental resilience ensures sustained antimicrobial action in physiologically relevant infection microenvironments, underscoring its significant clinical applicability.

3.6 *In vivo* therapeutic efficacy of $AuCu_3/H_2O_2$ in murine wound infection and human otitis externa

3.6.1 *Therapeutic efficacy of $AuCu_3/H_2O_2$ on infected skin wound by PR-CRKP in animal model*

To further investigate the bactericidal efficacy of $AuCu_3/H_2O_2$ within a complex organism, a murine skin wound infection model induced by PR-CRKP was established. In the absence of bacterial infection, skin wounds in mice typically healed by day 8, although minor scarring was observed. Histological examination via H&E staining revealed disorganization of the subepidermal architecture (Fig. 5(a)). In contrast, wounds infected with PR-CRKP failed to heal by day 8, presenting with ulcers and significant scarring,

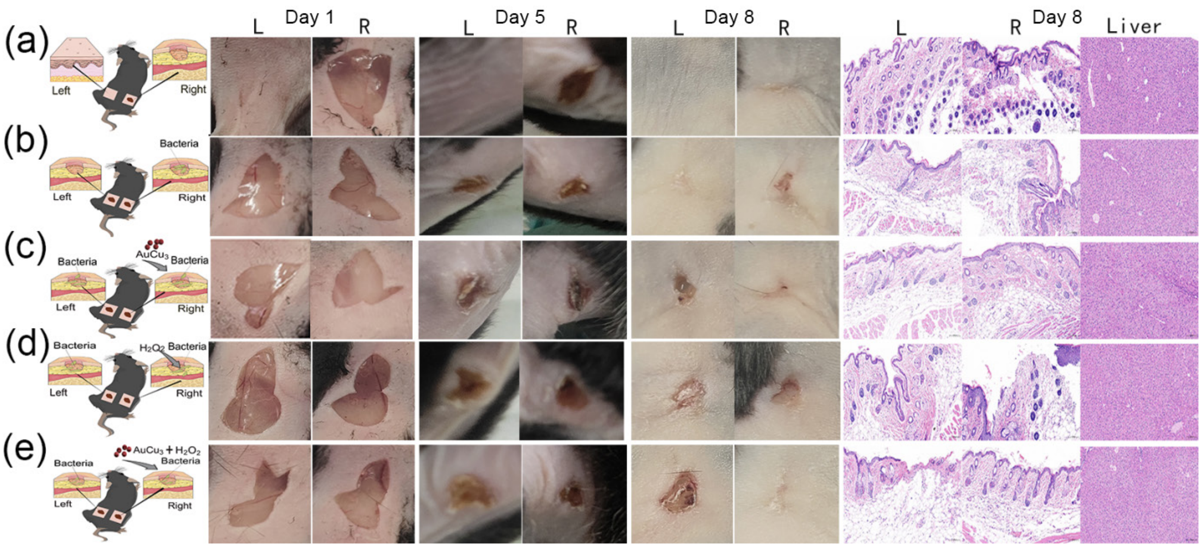

Figure 5 $AuCu_3$ and $AuCu_3/H_2O_2$ therapy promote wound healing in a murine model of PR-CRKP Infection. (a)–(e) Left: schematic of the experimental design, the left dorsal skin wound on the same mouse served as the control, while the right dorsal skin wound received the experimental treatment; middle: representative wound appearance on days 1, 5, and 8; right: H&E-stained histopathological sections of wound tissues harvested on day 8. (a) Uninfected control, (b) PR-CRKP-infected and untreated, (c) infected and treated with $AuCu_3$, (d) infected and treated with H_2O_2, and (e) infected and treated with $AuCu_3/H_2O_2$ combination.

alongside disrupted subcutaneous structure (Fig. 5(b)). Daily treatment with $AuCu_3$ alone after PR-CRKP infection led to complete wound closure by day 8, although with scar formation; this outcome was markedly superior to that of the untreated infection control (Fig. 5(c)). Treatment with H_2O_2 alone, however, not only prevented healing but also exacerbated tissue damage, as evidenced by complete epidermal disruption and severe deterioration of the underlying structure (Fig. 5(d)). Notably, combined treatment with $AuCu_3/H_2O_2$ led to complete wound closure by day 8 without visible scarring, closely resembling the natural healing process of uninfected controls. H&E staining confirmed full epidermal regeneration and well-organized, intact subcutaneous tissues (Fig. 5(e)). Furthermore, no signs of systemic toxicity were observed in $AuCu_3$-treated mice, as indicated by unaltered body weight (Fig. S3 in the ESM), normal coat condition, and normal liver histology (Fig. 5). In summary, these findings demonstrate that $AuCu_3$ monotherapy promotes the healing of infected wounds, while the $AuCu_3/H_2O_2$ combination yields optimal outcomes, facilitating tissue regeneration with minimal scar formation. Notably, no acute drug toxicity was observed.

3.6.2 Therapeutic efficacy of $AuCu_3/H_2O_2$ against S. aureus-induced otitis externa in human case

Otitis externa is a highly common infection of the human auditory canal, with contributing factors including detrimental habits like frequent scratching (pruritus). A case of voluntary $AuCu_3$ application for human otitis externa was documented (Fig. 6). The initial onset occurred in the right ear on July 22, 2025, presenting with pain and swelling; symptoms alleviated following povidone-iodine disinfection. The left ear became affected on July 28, 2025, with progressive symptom worsening. By July 30, the right ear exhibited only a minor, slightly raised furuncle with mild tenderness, consistent with mild otitis externa. In contrast, the left ear displayed two distinct masses and one ulcer, accompanied by significant pain and severe clinical manifestations. On July 31, the severely affected left ear was treated topically three times daily with 50 μg/mL $AuCu_3$ plus 500 μM H_2O_2, while the milder right ear received 500 μM H_2O_2 alone on the same schedule. Within three days, the left ear treated with $AuCu_3/H_2O_2$ resolved completely; bacterial culture indicated normal skin flora, including *S. epidermidis* (Sep) and *S. aureus* (Sau). Conversely, the right ear treated with H_2O_2 alone worsened, showing severe diffuse swelling that distorted and narrowed the ear canal, accompanied by significant hearing impairment. Symptoms progressively extended to the right facial region and throat. Culture from this ear revealed a predominant growth of Sau. This infection was subsequently resolved after a one-week course of oral amoxicillin. Collectively, this clinical case indicates that $AuCu_3/H_2O_2$ exhibits potent antibacterial, anti-edema, and ulcer-healing properties, with no perceived systemic toxicity in this instance. Although H_2O_2 is commonly used as a skin disinfectant and in otitis treatments, its standalone application in this case of Sau-induced otitis externa appeared to exacerbate the infection, a result that can be explained by our earlier cytotoxicity data for H_2O_2.

The translational potential of $AuCu_3$ is strongly supported by these *in vivo* data. In a murine wound infection model, the $AuCu_3/H_2O_2$ combination not only eradicated the PR-CRKP infection but also promoted optimal wound healing with minimal scarring, closely resembling uninfected healing. This outcome sharply contrasted with the exacerbated tissue damage caused by H_2O_2 monotherapy, highlighting $AuCu_3$'s role in mitigating H_2O_2-induced cytotoxicity and enabling effective sterilization at safe H_2O_2 doses. The excellent biocompatibility of $AuCu_3$, confirmed by the absence of systemic toxicity in treated mice, is a crucial attribute for clinical application [30]. Perhaps the most compelling evidence for clinical potential comes from a documented human case of Sau otitis externa. The differential treatment outcome—complete resolution with $AuCu_3/H_2O_2$ versus clinical deterioration with H_2O_2 alone—provides a direct, real-world validation of our *in vitro* and *in vivo* findings. Contrary to its conventional use, $\leq$ 3% H_2O_2 exacerbated infections and delayed healing in skin wounds, whereas the $AuCu_3$-catalyzed system proved safe and effective. The nanozyme's rapid, localized conversion of H_2O_2 into ·OH ensures potent bacterial killing without host damage [9]. This "catalytic

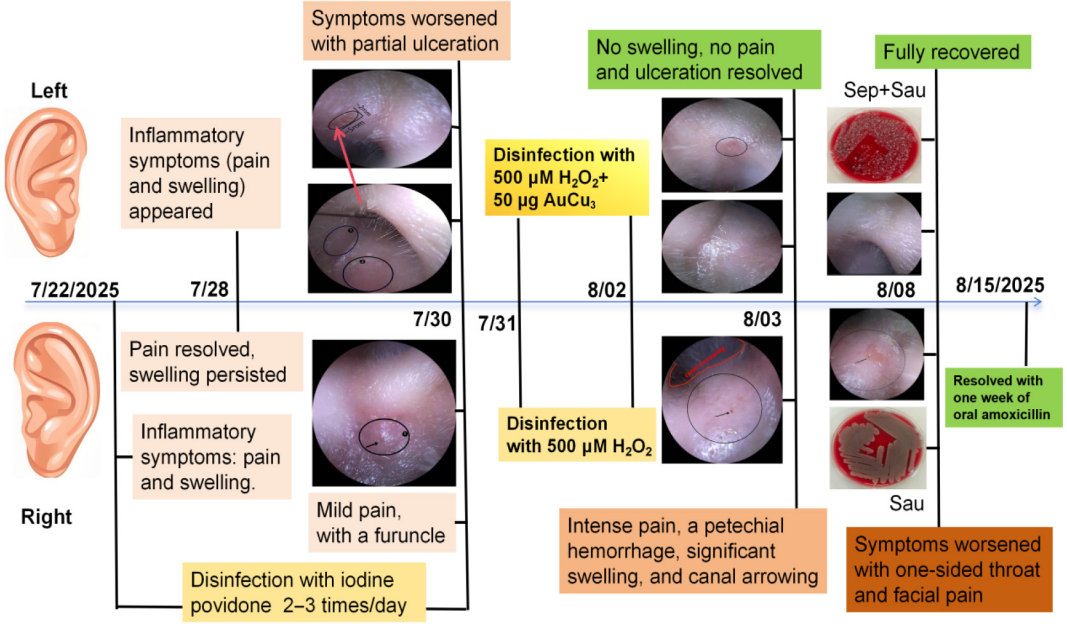

Figure 6 A clinical case report on the efficacy of $AuCu_3/H_2O_2$ in treating human otitis externa.

containment" effect robustly promotes wound healing *in vivo*, demonstrating potent antibacterial, anti-edema, and tissue-repairing properties without observed adverse effects, thereby validating the high translational value of this approach. Finally, the reusability of the $AuCu_3$ nanozyme, albeit with slight reduction likely due to physical handling loss, suggests potential for cost-effective and sustained catalytic applications, further enhancing its practical value.

3.7 The mechanism of $AuCu_3$ for promoting wound healing

Given that our *in vivo* results showed $AuCu_3$ alone promotes wound healing without H_2O_2, we posit that it facilitates healing not only by catalyzing H_2O_2 for sterilization but also by modulating cellular functions. To investigate this, we subjected $AuCu_3$-stimulated human peripheral blood mononuclear cells (PBMCs) to scRNA-seq with an emphasis on the monocyte-macrophage axis—the principal nano-processing hub in which blood-circulating monocytes extravasate, mature into macrophages, and subsequently internalize, metabolize, and immunologically orchestrate the response to nanoparticles—to unveil the pro-resolving/regenerative programs engaged (Fig. 7(a)). Our scRNA-seq analysis delineated the major immune cell lineages, including T cells, B cells, NK cells, and monocytes (TBNK), as evidenced by the distinct clustering in Fig. 7(b). Within the monocyte-macrophage system, we identified four distinct subsets based on canonical marker genes: CD14$^+$ monocytes (Mono_CD14), CD14$^+$CD16$^+$ monocytes (Mono_CD14_CD16), CD16$^+$ monocytes (Mono_CD16), and a macrophage population characterized by high expression of complement C1q C-chain (Macro_C1QC) (Figs. 7(c) and 7(d)). Comparative analysis revealed that $AuCu_3$ treatment did not significantly alter the proportional distribution of these TBNK or monocyte subsets compared to the control group (Fig. S4 in the ESM). As illustrated in Fig. 7(e), compared to the control group, $AuCu_3$ treatment resulted in 45, 24, and 1 statistically significant differentially expressed genes (DEGs) in Mono_CD14, Mono_CD14_CD16, and Mono_CD16 monocytes, respectively. Given that Mono_CD14 exhibited the highest number of DEGs and represents a more mature functional state, the distribution characteristics of its DEGs are further displayed in Figs. 7(f) and 7(g). These DEGs could be categorized into functional groups such as immune cell migration and chemotaxis, copper metabolism, detoxification or homeostasis, energy metabolism, and biosynthesis. GO and KEGG pathway enrichment analyses revealed that these DEGs are predicted to activate signaling pathways that may induce chemotaxis and migration of immune cells—including monocytes, neutrophils, and eosinophils—enhance the conversion of ADP to ATP, and promote copper transport (Figs. 7(h) and 7(i)). Concurrently, these pathways appear to regulate transcriptional and translational processes, as well as detoxification mechanisms, thereby contributing to the maintenance of cellular homeostasis. As a result, $AuCu_3$ treatment not only potentiates monocyte immunofunction by elevating oxidative phosphorylation and promoting chemokine-mediated infiltration of innate immune cells for wound repair, but also supports cellular homeostasis through coordinated copper metabolic and detoxification pathways, thereby averting polarization or death (Fig. 7(j)).

Based on our integrated findings, we propose that $AuCu_3$ facilitates wound healing through a multifaceted mechanism centered on the functional reprogramming of monocytes, rather than by inducing cytotoxicity or altering immune subset proportions. scRNA-seq analysis identified the CD14$^+$ monocyte subset as the primary responsive population, exhibiting extensive transcriptional changes in pathways critical for immunometabolism and tissue repair. The metabolic shift from glycolysis to oxidative phosphorylation equips these cells with the bioenergetic capacity for sustained activity, driving key reprogramming events, including enhanced chemotaxis and monocyte-to-macrophage differentiation, which collectively aid inflammation resolution and tissue repair [31]. Moreover, $AuCu_3$-induced upregulation of chemotactic factors such as CCL2 (C-C motif chemokine ligand 2) and galectin-3 (encoded by *LGALS3*) orchestrates the coordinated recruitment of innate immune effectors (monocytes, neutrophils, and lymphocytes) to the wound site. This process is pivotal for the subsequent immune response: neutrophils and monocytes mediate potent bacterial clearance, while lymphocytes and monocytes

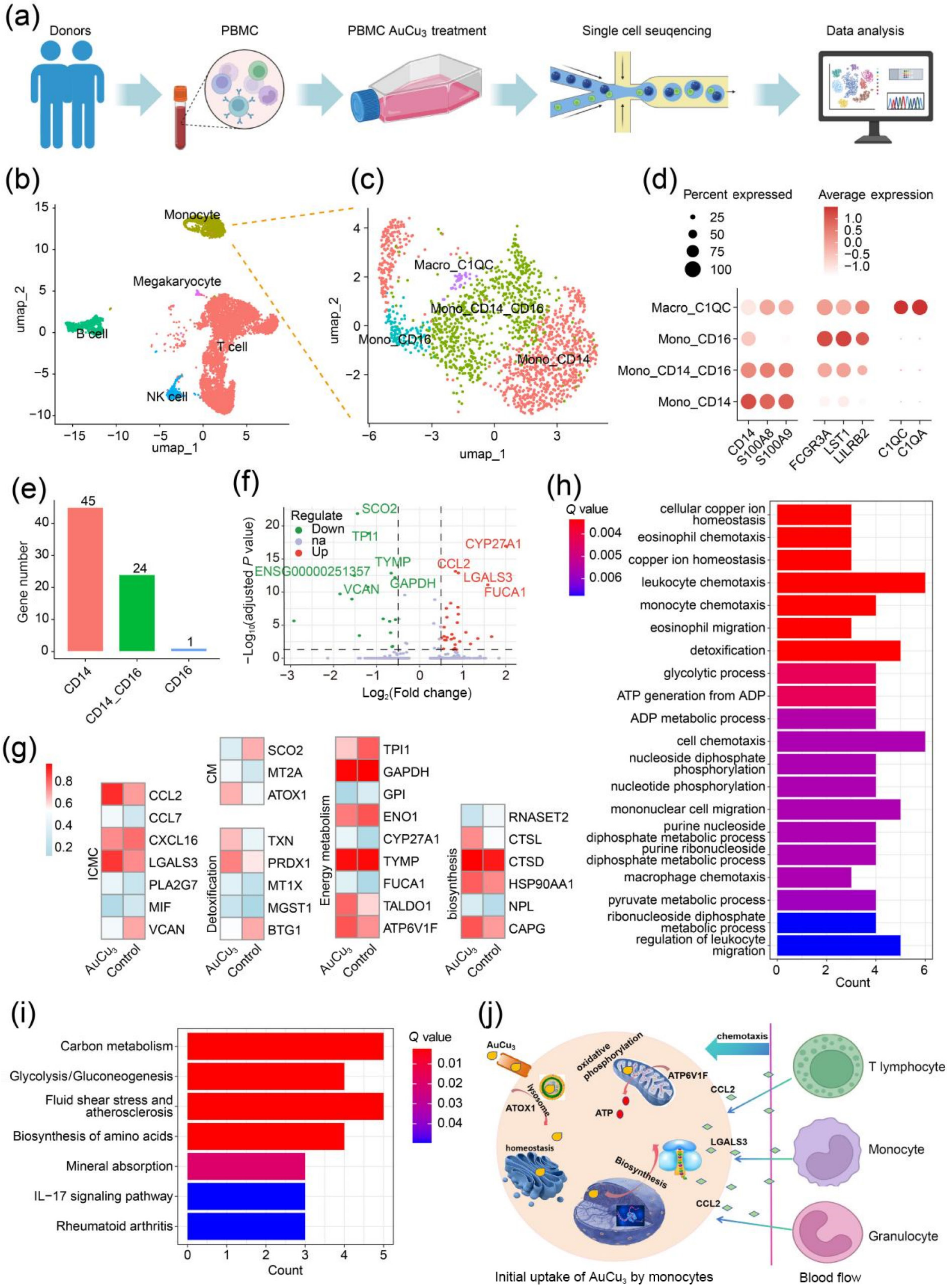

Figure 7 $AuCu_3$ potentiates monocyte chemotaxis and functional capacity to amplify immune cell recruitment in wound healing. (a) Primary human PBMCs were treated with $AuCu_3$ for 24 h and subsequently subjected to scRNA-seq. (b) The major immune cell types, including T cells, B cells, NK cells, and monocytes (denoted collectively as TBNK). (c) Subpopulation and (d) characteristic marker genes of monocytes. (e) Number of DEGs across subpopulations. (f) Volcano plots and (g) heatmap of DEGs on the $CD4^+$ monocytes between $AuCu_3$ and control, illustrating the average expression of key genes in chemotaxis, ATP synthesis, biosynthesis, copper metabolism, and detoxification homeostasis. (h) GO and (i) KEGG enrichment analysis of DEGs. (j) Diagram illustrating the mechanism by which treated monocytes are activated and promote the subsequent recruitment of immune cells to the wound site.

further contribute to inflammation resolution and tissue repair [32, 33]. The unique function of $AuCu_3$ has not been reported in current research. Although several studies have shown that certain metal nanoparticles, such as iron oxide nanoparticles, can modulate the activation of innate immune cells, the underlying mechanisms remain poorly understood [34, 35]. Furthermore, $AuCu_3$ engages copper metabolism and detoxification pathways to maintain cellular homeostasis during its catalytic activity. By achieving a precisely tuned balance between pro-healing inflammation and homeostatic control, $AuCu_3$ emerges as a promising therapeutic agent for promoting regenerative wound repair.

While this study provides comprehensive evidence for the efficacy of the $AuCu_3/H_2O_2$ system, several aspects warrant further investigation. The promising clinical outcome requires validation beyond a single case. A key mechanistic question is whether the observed standalone wound-healing promotion by $AuCu_3$ is mediated by the catalysis of trace endogenous H_2O_2 or by the active reprogramming of monocyte functions via specific key pathways [36]. Moreover, although no direct cytotoxicity was observed, a thorough investigation into long-term biocompatibility—including potential risks such as carcinogenicity and immune response modulation—is imperative. Finally, the long-term *in vivo* biodistribution, metabolism, and chronic toxicity of the nanoparticles, alongside the development of advanced formulations for targeted delivery, must be thoroughly evaluated to fully realize the therapeutic potential of this platform.

4 Conclusions

In conclusion, we have developed and rigorously validated an $AuCu_3$ nanozyme-based antibacterial platform that effectively addresses several key challenges in combating MDR bacterial infections. This platform bypasses existing resistance mechanisms, acts rapidly and broadly, achieves complete sterilization through a synergistic mechanism involving multilevel physicochemical and physiological regulation, and demonstrates excellent biocompatibility *in vivo*. Its clear clinical potential positions $AuCu_3$ nanozymes as a promising therapeutic candidate. Furthermore, the platform's potent bactericidal efficacy and reusability make it a safe and effective option for environmental decontamination in hospital settings, where it could help curb the spread of resistant pathogens.

Electronic Supplementary Material: Supplementary material (further details of the experimental procedures and data, including metal release kinetics, antimicrobial susceptibility testing (MIC and disk diffusion), nanozyme recycling assays, electron microscopy (spherical aberration-corrected TEM and HRTEM), ESR spectroscopy, *in vivo* body weight analysis, and single-cell RNA sequencing) is available in the online version of this article at https://doi.org/10.26599/NR.2026.94908625.

Data availability

All data needed to support the conclusions in the paper are presented in the ESM. Additional data related to this paper may be requested from the corresponding author upon request.

Acknowledgements

Funding: Suzhou Science and Technology Agency Project: No. SZM2024019; Suzhou Industrial Park Medical and Health Innovation Research Project: No. CXYJ2024A08; Suzhou Industrial Park Healthcare Talent Support Initiative: No. 202461/YQWS202510.

Declaration of competing interest

The authors declare that they have no known competing financial interests or personal relationships that could have appeared to influence the work reported in this paper.

Author contribution statement

Q. Z. H: Writing and editing the original draft, conceiving and designing the research. J. J. C., and W. W. S.: Conducting the majority of bactericidal experiments. J. H. Z.: Conducting cytotoxicity assays and checking the main text. J. M. Y.: Synthesis of the $AuCu_3$ nanoenzyme. X. J. F.: Supervising the research and providing nanomaterials. Z. T. C.: Conceiving the research. T. Z., and J. M. Z.: Preserving the strains and assisting with the experiments. M. L., T. F. W., and Z. Z. Y.: Investigation and visualization.

Informed consent

Written consent was waived, as all samples and infection interventions were voluntarily provided by the author Q. Z. H. No clinical trials or patient-derived samples were involved; only bacterial strains and animal models were used.

Ethics statement

Animal experiments were performed following the guidelines of the Institutional Committee for the Care and Use of Laboratory Animals of the Fourth Affiliated Hospital of Soochow University and approved by its Committee on Ethical Use of Animals (Approval No. 251224).

Use of AI statement

None.

References

[1] E.; Carrara, E.; Savoldi, A.; Harbarth, S.; Mendelson, M.; Monnet, D. L.; Pulcini, C.; Kahlmeter, G.; Kluytmans, J.; Carmeli, Y. et al. Discovery, research, and development of new antibiotics: The WHO priority list of antibiotic-resistant bacteria and tuberculosis. *Lancet Infect. Dis.* **2018**, *18*, 318–327.

[2] Wolford, H.; McCarthy, N. L.; Baggs, J.; Hatfield, K. M.; Maillis, A.; Olubajo, B.; Bishop, J.; Ferretti, M.; Craig, M. R.; Magill, S. S. et al. Antimicrobial-resistant infections in hospitalized patients. *JAMA Netw. Open* **2025**, *8*, e2462059.

[3] Wang, Q. J.; Zhou, L. J.; Chen, X. L.; Yao, J. Y.; Sun, X. R.; Peng, K.; Gao, Y. Y.; Feil, E. J.; Yu, Y. S.; Wang, Z. Q. et al. Global emergence and transmission dynamics of carbapenemase-producing *citrobacter freundii* sequence type 22 high-risk international clone: A retrospective, genomic, epidemiological study. *Lancet Microbe* **2025**, *6*, 101149.

[4] Lee, J.; Sunny, S.; Nazarian, E.; Fornek, M.; Abdallah, M.; Episcopia, B.; Rowlinson, M. C.; Quale, J. Carbapenem-resistant *Klebsiella pneumoniae* in large public acute-care healthcare system, New York, New York, USA, 2016-2022. *Emerg. Infect. Dis.* **2023**, *29*, 1973–1978.

[5] H.; Carrara, E.; Savoldi, A.; Hansen, P.; Garlasco, J.; Campagnaro, E.; Boccia, S.; Castillo-Polo, J. A.; Magrini, E.; Garcia-Vello, P. et al.

The WHO bacterial priority pathogens list 2024: A prioritisation study to guide research, development, and public health strategies against antimicrobial resistance. *Lancet Infect. Dis.* **2025**, *25*, 1033–1043.

[6] Jiang, B.; Guo, Z. J.; Liang, M. M. Recent progress in single-atom nanozymes research. *Nano Res.* **2023**, *16*, 1878–1889.

[7] Zhang, S. J.; Xu, R.; He, S. B.; Sun, R.; Wang, G. N.; Wei, S. Y.; Yan, X. Y.; Fan, K. L. Nanozyme-driven multifunctional dressings: Moving beyond enzyme-like catalysis in chronic wound treatment. *Military Med. Res.* **2025**, *12*, 27.

[8] Sheng, J. Y.; Wu, Y. H.; Ding, H.; Feng, K. Z.; Shen, Y.; Zhang, Y.; Gu, N. Multienzyme‐like nanozymes: Regulation, rational design, and application. *Adv. Mater.* **2024**, *36*, 2211210.

[9] Zheng, J. J.; Wang, X. Y.; Li, Z. Q.; Shen, X. M.; Wei, G.; Xia, P. F. H.; Zhou, Y. G.; Wei, H.; Gao, X. F. Integrated computational and experimental framework for inverse screening of candidate antibacterial nanomedicine. *ACS Nano* **2024**, *18*, 1531–1542.

[10] Zhang, N. L.; Chen, X.; Lu, Y. J.; An, L.; Li, X.; Xia, D. G.; Zhang, Z.; Li, J. X. Nano‐intermetallic $AuCu_3$ catalyst for oxygen reduction reaction: Performance and mechanism. *Small* **2014**, *10*, 2662–2669.

[11] Sra, A. K.; Schaak, R. E. Synthesis of atomically ordered AuCu and $AuCu_3$ nanocrystals from bimetallic nanoparticle precursors. *J. Am. Chem. Soc.* **2004**, *126*, 6667–6672.

[12] Wang, Y.; Sun, Q.; Zhang, Y.; Li, X. L.; Liang, Q. T.; Guo, R.; Zhang, L. Q.; Han, X. Q.; Wang, J.; Shao, L. et al. Systemic immune dysregulation in severe tuberculosis patients revealed by a single-cell transcriptome atlas. *J. Infect.* **2023**, *86*, 421–438.

[13] Wang, Y.; Luu, L. D. W.; Liu, S.; Zhu, X.; Huang, S. Y.; Li, F.; Huang, X. L.; Guo, L. Y.; Zhang, J.; Ge, H. Y. et al. Single-cell transcriptomic analysis reveals a systemic immune dysregulation in COVID-19-associated pediatric encephalopathy. *Sig. Transduct. Target. Ther.* **2023**, *8*, 398.

[14] Kumar, A.; Lee, I. S. Designer nanoreactors for bioorthogonal catalysis. *Acc. Chem. Res.* **2024**, *57*, 413–427.

[15] Wang, X. R.; Wang, W. X. Cu-based nanoparticle toxicity to zebrafish cells regulated by cellular discharges. *Environ. Pollut.* **2022**, *292*, 118296.

[16] Kus-Liśkiewicz, M.; Fickers, P.; Ben Tahar, I. Biocompatibility and cytotoxicity of gold nanoparticles: Recent advances in methodologies and regulations. *IJMS* **2021**, *22*, 10952.

[17] Bekeschus, S.; Liebelt, G.; Menz, J.; Singer, D.; Wende, K.; Schmidt, A. Cell Cycle-related genes associate with sensitivity to hydrogen peroxide-induced toxicity. *Redox Biol.* **2022**, *50*, 102234.

[18] Guzmán-Soto, I.; McTiernan, C.; Gonzalez-Gomez, M.; Ross, A.; Gupta, K.; Suuronen, E. J.; Mah, T. F.; Griffith, M.; Alarcon, E. I. Mimicking biofilm formation and development: Recent progress in *in vitro* and *in vivo* biofilm models. *iScience* **2021**, *24*, 102443.

[19] Wang, J. W.; Yu, Y.; Chen, L. Z.; Yu, J. Q.; Jin, X. Y.; Zeng, R. M.; Luo, X. M.; Cong, Y. G.; Xu, G. X.; Zhang, J. L. et al. NIR-triggered and glucose-powered hollow mesoporous Mo-based single-atom nanozymes for cascade chemodynamic diabetic infection therapy. *Mater. Today Bio* **2025**, *31*, 101557.

[20] Elbaiomy, R. G.; El‐Sappah, A. H.; Guo, R.; Luo, X. L.; Deng, S. Y.; Du, M. F.; Jian, X. H.; Bakeer, M.; Li, Z. X.; Zhang, Z. Antibiotic resistance: A genetic and physiological perspective. *MedComm* **2025**, *6*, e70447.

[21] Choi, N.; Choi, E.; Cho, Y. J.; Kim, M. J.; Choi, H. W.; Lee, E. J. A shared mechanism of multidrug resistance in laboratory-evolved uropathogenic *Escherichia coli*. *Virulence* **2024**, *15*, 2367648.

[22] Escalona, A.; Hayashi, E.; Evans, M.; Van Bakel, H.; Alburquerque, B.; Dupper, A. C.; McBride, R.; Altman, D. R. Polymicrobial methicillin-resistant *Staphylococcus aureus* bloodstream infections. *Microbiol Spectr* **2024**, *12*, e0108124.

[23] Aslam, B.; Wang, W.; Arshad, M. I.; Khurshid, M.; Muzammil, S.; Rasool, M. H.; Nisar, M. A.; Alvi, R. F.; Aslam, M. A.; Qamar, M. U. et al. Antibiotic resistance: A rundown of a global crisis. *Infect. Drug Resist.* **2018**, *11*, 1645–1658.

[24] Generalova, A. N.; Dushina, A. O. Metal/metal oxide nanoparticles with antibacterial activity and their potential to disrupt bacterial biofilms: Recent advances with emphasis on the underlying mechanisms. *Adv. Colloid Interface Sci.* **2025**, *345*, 103626.

[25] Zhydzetski, A.; Głowacka-Grzyb, Z.; Bukowski, M.; Żądło, T.; Bonar, E.; Władyka, B. Agents targeting the bacterial cell wall as tools to combat gram-positive pathogens. *Molecules* **2024**, *29*, 4065.

[26] Markowska-Szczupak, A.; Wróbel, R. J.; Kiełbus-Rąpała, A.; Michalkiewicz, B. Durable antibacterial performance of Au–Ag–Cu thin films prepared by magnetron sputtering: Real-world applications. *Molecules* **2025**, *30*, 3348.

[27] Li, J. R.; Wang, H. B.; Gao, P.; Wang, R. M.; Chan, C. L.; Yi-Tsun Kao, R.; Li, H. Y.; Sun, H. Z. Bismuth drug eradicates multi-drug resistant *Burkholderia cepacia* complex via aerobic respiration. *Chem. Sci.* **2025**, *16*, 12372–12384.

[28] Vaiwala, R.; Sharma, P.; Ganapathy Ayappa, K. Differentiating interactions of antimicrobials with gram-negative and gram-positive bacterial cell walls using molecular dynamics simulations. *Biointerphases* **2022**, *17*, 061008.

[29] Evans, L.; Rhodes, A.; Alhazzani, W.; Antonelli, M.; Coopersmith, C. M.; French, C.; Machado, F. R.; Mcintyre, L.; Ostermann, M.; Prescott, H. C. et al. Surviving sepsis campaign: International guidelines for management of sepsis and septic shock 2021. *Intensive Care Med.* **2021**, *47*, 1181–1247.

[30] Zhang, Y. X.; Gao, Y.; Li, N.; Xu, L. Y.; Wang, Y. J.; Liu, H. Z. Polypropylene sulfide methotrexate nanoparticles target the synovial lymphatic system to restore immune tolerance in rheumatoid arthritis. *Int. J. Pharm.* **2024**, *665*, 124713.

[31] Purvis, G. S. D.; McNeill, E.; Wright, B.; Channon, K. M.; Greaves, D. R. Ly6Chi monocytes are metabolically reprogrammed in the blood during inflammatory stimulation and require intact OxPhos for chemotaxis and monocyte to macrophage differentiation. *Cells* **2024**, *13*, 916.

[32] Gschwandtner, M.; Derler, R.; Midwood, K. S. More than just attractive: How CCL2 influences myeloid cell behavior beyond chemotaxis. *Front. Immunol.* **2019**, *10*, 2759.

[33] Di Gregoli, K.; Somerville, M.; Bianco, R.; Thomas, A. C.; Frankow, A.; Newby, A. C.; George, S. J.; Jackson, C. L.; Johnson, J. L. Galectin-3 identifies a subset of macrophages with a potential beneficial role in atherosclerosis. *ATVB* **2020**, *40*, 1491–1509.

[34] Wu, Q.; Jin, R.; Feng, T.; Liu, L.; Yang, L.; Tao, Y. H.; Anderson, J. M.; Ai, H.; Li, H. Iron oxide nanoparticles and induced autophagy in human monocytes. *Int. J. Nanomedicine* **2017**, *12*, 3993–4005.

[35] Zhang, J. H.; Ji, C.; Zhang, H. B.; Shi, H.; Mao, F.; Qian, H.; Xu, W. R.; Wang, D. Q.; Pan, J. M.; Fang, X. J. et al. Engineered neutrophil-derived exosome-like vesicles for targeted cancer therapy. *Sci. Adv.* **2022**, *8*, eabj8207.

[36] Tan, X. F.; Lin, N. Y.; Yang, S.; Gong, H. Y.; Wang, M. H.; Li, N.; Liu, F.; Rao, D. J.; Wu, Y. Y.; Tang, J. et al. AuCu@CuO_2 aerogels with H_2O_2/O_2 self-supplying and quadruple enzyme-like activity for MRSA-infected diabetic wound management. *Adv. Sci.* **2025**, *12*, e2502391.